

Received January 9, 2020, accepted January 20, 2020, date of publication January 23, 2020, date of current version February 11, 2020.

Digital Object Identifier 10.1109/ACCESS.2020.2969085

Neural Learning Enhanced Variable Admittance Control for Human–Robot Collaboration

XIONGJUN CHEN¹, NING WANG², (Member, IEEE),
HONG CHENG³, (Senior Member, IEEE), AND
CHENGUANG YANG², (Senior Member, IEEE)

¹College of Automation Science and Engineering, South China University of Technology, Guangzhou 510640, China

²Bristol Robotics Laboratory, University of the West of England, Bristol BS16 1QY, U.K.

³Center for Robotics, University of Electronic Science and Technology of China, Chengdu 611731, China

Corresponding author: Chenguang Yang (cyang@ieee.org)

This work was supported in part by the Engineering and Physical Sciences Research Council (EPSRC) under Grant EP/S001913.

ABSTRACT In this paper, we propose a novel strategy for human-robot impedance mapping to realize an effective execution of human-robot collaboration. The endpoint stiffness of the human arm impedance is estimated according to the configurations of the human arm and the muscle activation levels of the upper arm. Inspired by the human adaptability in collaboration, a smooth stiffness mapping between the human arm endpoint and the robot arm joint is developed to inherit the human arm characteristics. The estimation of stiffness term is generalized to full impedance by additionally considering the damping and mass terms. Once the human arm impedance estimation is completed, a Linear Quadratic Regulator is employed for the calculation of the corresponding robot arm admittance model to match the estimated impedance parameters of the human arm. Under the variable admittance control, robot arm is governed to be compliant to the human arm impedance and the interaction force exerted by the human arm endpoint, thus the relatively optimal collaboration can be achieved. The radial basis function neural network is employed to compensate for the unknown dynamics to guarantee the performance of the controller. Comparative experiments have been conducted to verify the validity of the proposed technique.

INDEX TERMS Impedance estimated model, variable admittance control, physical human-robot collaboration, neural networks.

I. INTRODUCTION

Robot is expected to compliantly perform a lot of complicated tasks. To some extent, robots liberate humans from the mind-numbingly repetitive work routines. During the last decades, robots have become a significant part of factory production, assisting in repetitive and dangerous operations. In some cases, tasks are either too complex to automate or too heavy to manipulate manually. It is difficult to address this problem by humans working alone or by automated robots, which raises the demand for human-robot collaboration. In recent years, robots gradually participate in the daily life of humans and the collaboration between human and robot has attracted more and more attention in recent works, for the purpose of improving the safety and the reliability of the robot systems. Paper [1] presents a novel approach to estimate the motion intention of the operator and the unknown robot dynamics.

The associate editor coordinating the review of this manuscript and approving it for publication was Seyedali Mirjalili¹.

Paper [2] focuses on alerting and reducing the static joint torque overloading of a human partner. The work [3] designed a boundary controller with input backlash based on the infinite-dimensional dynamic model to achieve the flexible control aims. A major feature of human-robot collaboration is the ability to maintain flexibility. On one hand, the operator can properly reduce stress and fatigue with the help of robots, and to some extent enhance operator's capabilities. On the other hand, the operator can provide information and transfer skills to the robot, also playing the role of a supervisor of the robot. With the involvement of the human operator, the flexibility of the process increases, which is benefit to accomplish a number of tasks [4], [5].

The ideal collaboration between humans and robots is that there is no separation and no guardrail. Therefore, a safer and more effective control strategy is needed for optimal human-robot collaboration (HRC). Impedance control [6], [7], hybrid force/position control [8] and iterative learning control [9] are the most discussed control approaches in

HRC systems. Hybrid force/position control is based on partitioning the control problem into position constraints along the normals of a generalized surface and force constraints along the tangents [10]. Iterative learning control is widely used to suppress vibrations, track target trajectories, and reject time-varying disturbances [11]. Compared with hybrid force/position control and iterative learning control, impedance control is adaptable to the transition between free motion and constrained motion, and it shows satisfied tracking capability when the external constraints are known. There are two possible forms of impedance control, one is impedance control based on robot endpoint position control, i.e., admittance control, and the other is impedance control based on torque control in joint space [12].

Admittance control is an alternative method of impedance control, when external forces exerted by the operator are measured as input and positions are taken as feedback to the operator. In [13], a neuroadaptive admittance controller is designed and makes the robot to behave like a prescribed admittance model. Research [14] presents a variable admittance control approach based on the inference of human intentions. In the scenarios of human-robot collaboration, in order to obtain an admittance model of robot, the estimation of impedance parameters of the human should be considered [15]. Research [15] presents a thought of the mapping between unknown environment dynamics and the robot admittance model. The acquisition process of the impedance parameters can be found in [16], [17]. Reference [17] denotes that the robot arm damping term is regarded as be proportional to the human arm stiffness item. References [16], [17] show that adjusting the admittance model parameters of the robot arm based on the impedance parameters of the human arm is a effective approach to enhance the performance of human-robot collaboration.

There are many ways to obtain information from the human-robot collaboration process, such as visual feedback [18], [19], bio-signals [20]–[22], language commands [23]. Using a force sensor on the robot to detect the objective of the operator to control the collaboration force has been explored in many applications [24], [25]. In some situations, the high-level information feedback could be prevented in a complex task. Electromyography (EMG) signals have been widely used to obtain the human intentions in human-robot collaboration tasks [26], [27]. The EMG signals extracted from the Biceps and Triceps are adopted to estimate and regulate the human impedance profiles [28].

Since the desired position is the output of the admittance control model, the performance of the human-robot collaboration also counts on the accuracy of the trajectory controller that contains the dynamics of the robot system. It's well known that a model-based controller can perform satisfying enough with an accurate model of the robot. However, the accurate model is difficult to be obtained due to the uncertainties [29]. In [30], a neural network control method is presented to compensate for the unknown dynamics. Radial basis function neural network (RBFNN) is adopted by [29] to

compensate for the system uncertainties. Radial basis function neural network has a relevantly small number of pairs of weights and thresholds to modify, and therefore training faster [31].

In this paper we propose a neural learning enhanced variable admittance control technique for human-robot collaboration. As mentioned above, the impedance parameters (i.e., stiffness, damping and mass) of the human arm need to be identified in order to obtain the desired admittance model of the robot arm. The human arm endpoint stiffness is estimated using the approach proposed in [32]. And we propose a stiffness mapping strategy between the human arm and the robot arm in order to achieve a more coordinated human-robot collaboration according to the estimated stiffness. Based on the stiffness estimation of the human arm, this paper considers all the impedance parameters to make the impedance estimation model completed. The off-line experimental results of the stiffness estimation process are used to estimate the damping term of the human arm impedance model. And the mass term is regarded as a constant near a predetermined range [28]. Since the human arm impedance parameters are fully obtained, a Linear Quadratic Regulator (LQR) is employed to obtain the required robot arm admittance model matching to the impedance parameters of the human arm [33]. The Riccati equation is solved to obtain the estimates of the parameters of the robot arm admittance model [34]. Once the admittance model of the robot arm is obtained, the expected relationship between the interaction force and displacement of the robot arm end-effector can be obtained. As the desired trajectory of the robot arm end-effector is obtained based on the admittance model, the robotics inverse kinematics (IK) is employed to calculate the desired joint angles. Since the uncertainties of dynamic parameters of the robot arm always exist, we designed a NN-based controller to enhance the performance of the human-robot collaboration in order to compensate for the effect caused by the dynamic environments.

The chosen task of robot collaborating with human to saw a wood can be a suitable way to verify the proposed method, which required a good coordination between the robot arm and the human arm. The stiffness mapping, the control of interaction force between robot arm end-effector and human arm endpoint and the accurate tracking of the desired positions are the key points to obtain a relatively optimal human-robot collaboration. The preliminary results of the study were presents at 2017 IEEE International Conference on Automation Science and Engineering [35] and this paper aims to supplement and enhance the method and present results of different experimental scenarios to enhance the persuasiveness.

The main contribution of this paper can be summarized as follows: 1) This paper proposes a novel framework for human-robot interaction, i.e., a human-robot impedance mapping strategy and variable admittance control based on the estimated human arm impedance parameters. 2) An NN-based controller is adopted to enhance the tracking performance

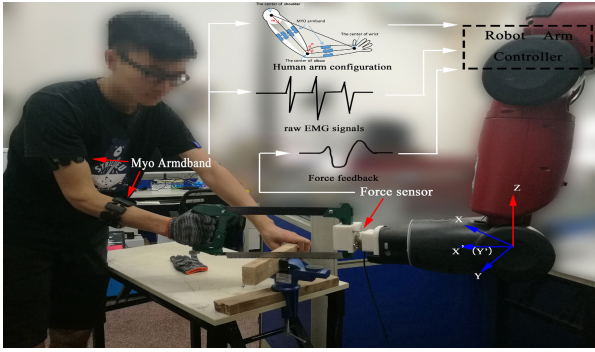


FIGURE 1. The overview of human-robot collaboration for the sawing task.

under the variable admittance control for human-robot collaboration.

The remainder of the paper is organized as follows. In section II, the acquisition of human arm impedance parameters and the stiffness mapping method are presented. In section III, the matching robot arm admittance model is obtained. In section IV, the NN-based controller is designed. In section V, the proposed technique is verified by experiments. Section VI concludes this paper.

II. IDENTIFICATION OF HUMAN ARM IMPEDANCE PARAMETERS

The proposed structure is shown in Fig. 1. The human arm configurations data and the raw electromyography signals are extracted from the Myo armbands. And the interaction force is detected by a force sensor attached at the robot arm end-effector. And these data mentioned above are applied to the manipulator’s controller after processing.

A. PRINCIPLE OF HUMAN ARM IMPEDANCE MODEL

Without loss of generality, the dynamic model of the human arm impedance can be described as follows:

$$M_H \ddot{x}_h + D_H \dot{x}_h + K_H x_h = F \quad (1)$$

where x_h , \dot{x}_h , \ddot{x}_h denotes the human arm endpoint position, velocity and acceleration, M_H , D_H and K_H represent the human arm mass, damping and stiffness terms. F denotes the interaction force.

The mass term M_H of human arm is regarded as a constant in the following description by ignoring the negligible effect of the muscle mass distribution on M_H in a certain range of a predetermined arm configuration [28]. A dimensionality-reduction estimation method of the human arm stiffness is utilized to estimate K_H in (1) [32].

$$K_H(p, q) = J_H^{+T}(q)[v(p)\overline{K}_J - G(q)]J_H^+(q) \quad (2)$$

where p is the co-activation index of upper arm muscles, q is the joint angle of human arm, $J_H(q)$ is the human arm Jacobian matrix, $v(p)$ is a muscle-activation-dependent index, \overline{K}_J is regarded as a constant matrix representing the human

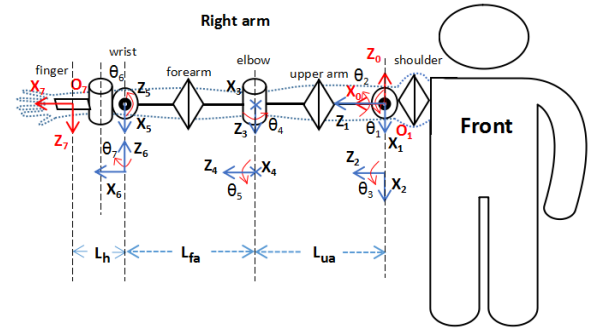


FIGURE 2. The human arm D-H model. (modified from [36]).

arm minimal joint stiffness. $G(q) = \frac{\partial J_H^T(q)F}{\partial q}$, denotes the influence of the interaction forces on the stiffness transformation. In this representation, it is clear that the stiffness term would vary with different muscle activation levels and human arm configurations. In addition, the processing of damping matrix D_H is introduced in the next subsection.

B. ESTIMATION OF STIFFNESS MATRIX

According to [36], the human arm configurations can be determined by three parameters of a triangle model, i.e., the direction of human arm plane, the direction of upper arm, and the angle between forearm and upper arm.

As shown in Fig. 2, a representative human arm Denavit-Hartenberg (D-H) model [37] is modified to denote the simplified human arm kinematics. The base coordinate is located at the shoulder. Direction x_0 and z_0 represent the axis of the frame, horizontal right and horizontal upwards. L_{ua} and L_{fa} represent the lengths of the upper arm and forearm. The angles of the first four joints, i.e., three shoulder joints and a single elbow joint can be calculated through IK algorithm [36].

Generally, we need to track the joint angles of the human arm to calculate the Jacobian matrix J_H . The real-time tracking of human arm joint angles can be achieved by transforming quaternions obtained by gyroscopes of Myo armbands to joint angles in a triangle model mention above. Therefore, the Jacobian matrix J_H of the human arm can be obtained according to the human arm D-H model shown in Fig. 2.

In order to identify the minimal joint stiffness matrix \overline{K}_J , multiple identification experiments are conducted with the classic perturbation method under different arm configurations and muscle activation levels (see [35] for details). The restoring force is measured by the force sensor and the dynamic relationship between the endpoint displacement of human arm and the recorded force is described as below [32],

$$F = \begin{bmatrix} F_{x_c} \\ F_{y_c} \\ F_{z_c} \end{bmatrix} = \begin{bmatrix} L_{xx} & L_{xy} & L_{xz} \\ L_{yx} & L_{yy} & L_{yz} \\ L_{zx} & L_{zy} & L_{zz} \end{bmatrix} \begin{bmatrix} \Delta X_c \\ \Delta Y_c \\ \Delta Z_c \end{bmatrix} \quad (3)$$

where F_{x_c} , F_{y_c} and F_{z_c} denote the human arm endpoint interaction force and ΔX_c , ΔY_c and ΔZ_c denote the displacement of the endpoint. And we employed a second-order linear

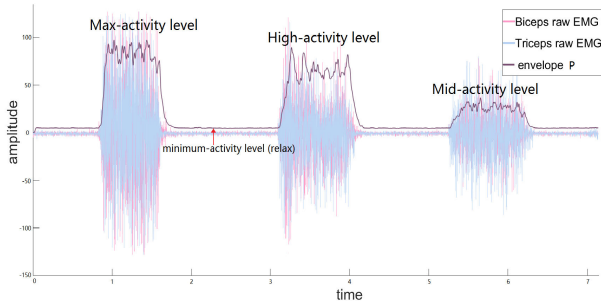


FIGURE 3. The envelope extracted from EMG signals using the proposed method.

model to identify the transfer function L_{ij} ,

$$L_{ij} = M_{Hij}s^2 + D_{Hij}s + K_{Hij}, \quad s = 2\pi f\sqrt{-1} \quad (4)$$

The parameters M_H , D_H and K_H of the transformation function L are identified using the least squares method. Consequently, all the stiffness matrices K_H identified by (4) using the minimum co-activation level experimental results are utilized to obtain the \overline{K}_J by minimizing the Frobenius norm below,

$$\| \overline{K}_J - J_H^T(q)K_H(p, q)J_H(q) - G(q) \| \quad (5)$$

In addition, the co-activation index p of upper arm muscles is obtained through the following method. As shown in Fig. 3, the envelope is extracted from the EMG signals using a moving average process and a low-pass filter. We use only two channels close to the Triceps and Biceps for convenience. Therefore, the equation below is used to indicate co-activation level p of the upper arm muscles,

$$p(s_p) = \frac{1}{W_s} \left(\sum_{s_p=1}^{W_s-1} A_B(t - s_p) + \sum_{s_p=1}^{W_s-1} A_T(t - s_p) \right) \quad (6)$$

where W_s is a predetermined window size, A_B and A_T are the amplitude of p , s_p and t represent the current sample point and sampling time.

Furthermore, the restoring force and the human arm endpoint displacement recorded from experiments with medium and high co-activation levels are employed to calculate the constant parameters of $v(p)$ in (8), i.e., χ_1 and χ_2 , by minimizing the Frobenius norm in (7).

$$\| v(p)\overline{K}_J - J_H^T(q)K_H(p, q)J_H(q) - G(q) \| \quad (7)$$

$$v(p) = -\frac{\chi_1[e^{-\chi_2 p} - 1]}{e^{-\chi_2 p} + 1} + 1 \quad (8)$$

Therefore, the human arm endpoint stiffness matrix K_H is calculated on-line using (2) as the human arm Jacobian matrix J_H , the muscle-activation-dependent index $v(p)$ and the minimal joint stiffness matrix \overline{K}_J are obtained.

Utilizing (3) and (4), all the damping matrices D_H of the minimum-activity, mid-activity and high-activity level trails can be obtained. Based on the analysis of the off-line experimental results of the damping matrices, it can be observed

that the variation of the damping value is not obvious within a certain range of the muscle activation level centered at each level. Corresponding to different muscle-activation-dependent index $v(p)$ in each arm configuration, we consider that the continuous numerical curve of the damping term can be discretized into variable constant matrices based on analysis and observation of the off-line experiment results. Therefore, a look-up table among the damping matrices, arm configurations, and the muscle activation levels in a certain range according to the off-line experimental results can be established. In the human-robot sawing scenario, the human arm configuration can be kept to only change in a small range while the muscle activation level is required to change in a wide range. Therefore, the look-up table can only consider the corresponding relations between the muscle activation levels and the obtained damping matrices.

C. STIFFNESS MAPPING BETWEEN HUMAN AND ROBOT ARM

Generally, the interaction force F transform to torque τ_c for control in joint space according to $\tau = J_r^T F$. Therefore, the stiffness in joint space of the cooperative robot arm can be derived from the human arm endpoint stiffness in Cartesian space according to the equation below [26],

$$K_r^q \approx J_r^T K_H J_r \quad (9)$$

where K_r^q denotes the mapping joint stiffness of robot arm, and J_r is the robot arm Jacobian matrix. The symbol of approximate equal means that the joint stiffness of robot arm is mapping from the endpoint stiffness of human arm, not exactly mapping from the endpoint stiffness of robot arm.

For the purpose of realizing a human-robot collaboration with master-slave conversion, stiffness mapping between the human arm and the robot arm should be adjusted. The stiffness mapping strategy is adjusted as below,

$$K_r^q \approx K_r^a - J_r^T K_H J_r \quad (10)$$

where K_r^a is a constant stiffness matrix for adjustment. With the help of the time-varying human arm endpoint stiffness and the adjustment factor, the mapping robot arm joint stiffness can be obtained. In addition, for the stability of the robot arm, limitation range of the robot arm joint stiffness are presented as $K_{min} \leq K_r^q \leq K_{max}$. K_{max} and K_{min} are the maximum stiffness and the minimum stiffness of the given range of the robot arm.

We employ a PD controller with variable gains to drive the robot arm cooperating with the human arm under a good tracking performance,

$$\tau_r = D(\dot{q}_d - \dot{q}) + K_r^q(q_d - q) \quad (11)$$

where τ_r is the control input of the robot arm, q_d and q represent the desired robot arm joint position and actual joint position. $D = k_s K_r^q$, with a properly chosen scale factor k_s , $k_s = [k_{s1}, k_{s2}, k_{s3}, \dots, k_{sn}]$, n represents the robot arm DOFs.

III. VARIABLE ADMITTANCE CONTROL MODEL

Generally, a typical dynamic equation of robot end-effector which is realized by admittance control is described as below:

$$F = I_r \ddot{x} + D_r \dot{x} + K_r(x - x_0) \quad (12)$$

where F denotes the interaction force, x , \dot{x} and \ddot{x} denote the robot arm position velocity and acceleration, x_0 is the initial position of the robot arm end-effector, I_r , D_r and K_r are desired virtual inertia, damping and stiffness matrices, respectively. In practical implementations, (12) is modified as a more simplified model retaining stiffness and damping,

$$F = D_r \dot{x} + K_r(x - x_0) \quad (13)$$

Considering a general time-invariant linear system as below,

$$\dot{\zeta} = X\zeta(t) + Yu(t) \quad (14)$$

where ζ represents the robot arm state, $u(t)$ is the system input at t time, X and Y are defined as known matrices. In addition, the robot arm state ζ is defined as below,

$$\zeta = [\dot{x}^T \ x^T \ \delta^T]^T \quad (15)$$

where δ denotes the state of a linear system to generate the reference task goal, x_f , which provides the feasibility to implement the optimized trajectory tracking. In particular, this linear system is described below,

$$\begin{cases} \dot{\delta} = U - \delta \\ x_f = V\delta \end{cases} \quad (16)$$

where U and V are known matrices needed to be determined. Considering the human arm state (1), the matrix X and Y are defined as below in order to match the corresponding impedance parameters of human arm,

$$X = \begin{bmatrix} -M_H^{-1}D_H & -M_H^{-1}K_H & 0 \\ I_n & 0 & 0 \\ 0 & 0 & U \end{bmatrix} \quad Y = \begin{bmatrix} -M_H^{-1} \\ 0 \\ 0 \end{bmatrix} \quad (17)$$

The mass, damping and stiffness of the human arm are all included in the matrices X and Y , which are then used to solve the desired admittance model. Furthermore, a LQR is employed to minimize the cost function below [33], [34]

$$C = \int_0^\infty [\dot{x}^T Q_1 \dot{x} + (x - x_f)^T Q_2 (x - x_f) + u^T R u] dt \quad (18)$$

where R , Q_2 and Q_1 represents the input of the system, the trajectory tracking error, and the velocity weighting matrices.

Based on the equation (15), (16) and (18), the cost function (18) can be rewritten as below,

$$C = \int_0^\infty [\dot{\zeta}^T Q \dot{\zeta} + u^T R u] dt \quad (19)$$

where

$$Q = \begin{bmatrix} Q_1 & 0 & 0 \\ 0 & Q_2 & -Q_2 V \\ 0 & -V^T Q_2 & V^T Q_2 V \end{bmatrix}.$$

The essence of the LQR is to obtain an optimal feedback of the system to minimize the cost function (19). According to this, the system input of the robot arm is defined as follows,

$$u = -K_f \zeta \quad (20)$$

where K_f is a state feedback gain matrix.

Using the interaction force F as the input u defined in (20). To understand (20) in the sense of admittance control, we assume that the optimal control has been achieved, and the desired admittance model is described as

$$\begin{aligned} F &= -K_f \zeta = -R^{-1} B^T P \zeta \\ &= -R^{-1} P_{11} \dot{x} - R^{-1} P_{12} x - R^{-1} P_{13} (V^T V)^{-1} x_f \end{aligned} \quad (21)$$

where P_{11} , P_{12} and P_{13} denote the three submatrices in the first row of the matrix P , which is the solution of the following equation:

$$P X + X^T P - P Y R^{-1} Y^T P + Q = 0 \quad (22)$$

According to the measured interaction force and a predetermined reference task goal, the desired trajectory and velocity of the robot arm end-effector can be calculated. And we can utilize the robotic IK algorithm to obtain the desired robot arm joint trajectory q_d .

IV. ADAPTIVE NEURAL NETWORK CONTROLLER

In order to enhance the tracking performance, we employed a neural network based controller to combine with the PD controller. The control torque generated by the NN-based controller is utilized to compensate for the dynamics uncertainties. The compensate torque τ_c is add to the control input τ_r to track the desired joint trajectory q_d obtained from the admittance control model.

Generally, the robot arm dynamics can be described as below,

$$M_r(q)\ddot{q} + C_r(q, \dot{q})\dot{q} + G_r(q) = \tau - \tau_{ext} \quad (23)$$

where M_r denotes the inertia matrix, C_r is the Coriolis matrix, G_r represents the gravity term, $\tau = \tau_c + \tau_r$ denotes the required torque for controlling and τ_{ext} denotes the external torque caused by payloads. \ddot{q} , \dot{q} , q denote the acceleration, velocity and position of the joint, respectively.

A. DESCRIPTION OF RADIAL BASIS FUNCTION NEURAL NETWORK

RBFNN have been proven to be capable of approximating any continuous function $\eta(\varepsilon) : R^m \rightarrow R$ in a number of researches,

$$\eta(\varepsilon) = W^T E(\varepsilon) + \varrho_\eta, \quad \forall \varepsilon \in \Omega_\varepsilon \quad (24)$$

where $\varepsilon \in \Omega_\varepsilon \subset R^m$ denotes the input factor, $W = [\omega_1, \omega_2, \dots, \omega_n]^T \in R^n$ is the constant NN weight vector, ϱ_η is the approximation error, $E(\varepsilon) = [e_1(\varepsilon), e_2(\varepsilon), \dots, e_n(\varepsilon)]^T \in R^n$ is the basis function and Gaussian functions are employed to defined $e_i(\varepsilon)$ as below,

$$e_i(\varepsilon) = \exp\left[\frac{(\varepsilon - v_i)^T (\varepsilon - v_i)}{-\psi_i^2}\right], \quad i = 1, 2, 3, \dots, n \quad (25)$$

where $v_i = [v_{i1}, v_{i2}, \dots, v_{im}] \in R^m$ denotes the note centers of Gaussian functions and ψ_i denotes the variance. In addition, we define the ideal weight vector as below

$$W = \arg \min\{\sup|\eta(\varepsilon) - W^T E(\varepsilon)|\}, \eta \in \Omega_\eta, W' \in R^n \quad (26)$$

Generally, the approximation error ϱ_η can be reduced arbitrarily small under this process.

B. ADAPTIVE CONTROLLER WITH NEURAL-LEARNING

The adaptive controller is designed to control the robot arm joint trajectory. Some definitions are defined as $e_q = q - q_d$, $s = \dot{e}_q + \Lambda e_q$, $v = \dot{q}_d - \Lambda e_q$, q and q_d are the robot arm actual and desired joint position, respectively, $\Lambda = \text{diag}(k_{s1}, k_{s2}, k_{s3}, \dots, k_{sn})$, k_{sn} represent the scale factor. Based on equation (23), we have

$$M_r \dot{s} + M_r \dot{v} + C_r s + C_r v + G_r = \tau - \tau_{ext} \quad (27)$$

According to (27), the required torque is designed as below

$$\tau = \widehat{M}_r \dot{v} + \widehat{C}_r v + \widehat{G}_r + \widehat{f} + \tau_{ext} - K_r^q s \quad (28)$$

where $\widehat{M}_r, \widehat{C}_r, \widehat{G}_r, \widehat{f}$ denote the estimated matrices of the robot arm inertia matrix, Coriolis matrix and gravity terms, and $f = \varrho_{M_r} \dot{v} + \varrho_{C_r} v + \varrho_{G_r}$. As we can see, the designed required torque τ consist of $\tau_c, \tau_r = -K_r^q s$ and τ_{ext} .

Based on (27) and (28), the robot arm close-loop dynamics can be obtained as below,

$$M_r \dot{s} + C_r s + K_r^q s - \widehat{f} = -(M_r - \widehat{M}_r) \dot{v} - (C_r - \widehat{C}_r) v - (G_r - \widehat{G}_r) \quad (29)$$

The RBFNN is employed to the approximation of M_r, C_r, G_r and f , and we obtain

$$\begin{aligned} M_r &= W_{M_r}^T E_{M_r} + \varrho_{M_r}, C_r = W_{C_r}^T E_{C_r} + \varrho_{C_r} \\ G_r &= W_{G_r}^T E_{G_r} + \varrho_{G_r}, f = W_f^T E_f + \varrho_f \end{aligned} \quad (30)$$

where $W_{M_r} = [W_{M_r,ij}], W_{C_r} = [W_{C_r,ij}], W_{G_r} = \text{diag}(W_{G_r,i})$ and $W_f = \text{diag}(W_{f,i})$ denote the ideal NN weight matrices. And $W_{M_r,ij} \in R^n, W_{C_r,ij} \in R^{2n}, W_{G_r,i} \in R^n$ and $W_{f,i} \in R^n, i, j = 1, 2, 3, \dots, n$, are defined as the weight matrices defined in (26). The basis function $E_{M_r}, E_{C_r}, E_{G_r}$ and E_f are designed as below,

$$\begin{aligned} E_{M_r}(q) &= \text{diag}(E_{q1}, E_{q2}, \dots, E_{qn}) \\ E_{C_r}(q, \dot{q}) &= \text{diag} \left(\begin{bmatrix} E_{q1} \\ E_{\dot{q}1} \end{bmatrix}, \dots, \begin{bmatrix} E_{qn} \\ E_{\dot{q}n} \end{bmatrix} \right) \\ E_{G_r} &= [E_{q1}^T, \dots, E_{qn}^T]^T \\ E_f(q, \dot{q}, v, \dot{v}) &= [\tilde{E}^T, \dots, \tilde{E}^T]^T \end{aligned} \quad (31)$$

where $E_{q1} = [e_1, e_2, \dots, e_n]^T \in R^n, E_{\dot{q}1} = [e_1(\dot{q}), e_2(\dot{q}), \dots, e_n(\dot{q})]^T \in R^n, \tilde{E} = [E_{q1}^T, E_{\dot{q}1}^T, E_{v1}^T, E_{\dot{v}1}^T]^T \in R^{4n}$, and $E_{v1} = [e_1(v), e_2(v), \dots, e_n(v)]^T \in R^n, E_{\dot{v}1} = [e_1(\dot{v}), e_2(\dot{v}), \dots, e_n(\dot{v})]^T \in R^n$. The NN-based estimates can be written as below, $\widehat{M}_r = \widehat{W}_{M_r}^T E_{M_r}, \widehat{C}_r = \widehat{W}_{C_r}^T E_{C_r}, \widehat{G}_r = \widehat{W}_{G_r}^T E_{G_r}$ and $\widehat{f}_r = \widehat{W}_f^T E_{f_r}$. Therefore, the (29) is

rewritten as below,

$$\begin{aligned} M_r \dot{s} + C_r s + K_r^q s &= -\widetilde{W}_{M_r}^T E_{M_r} \dot{v} - \widetilde{W}_{C_r}^T E_{C_r} v \\ &\quad - \widetilde{W}_{G_r}^T E_{G_r} - \widetilde{W}_f^T E_f - \varrho_f \end{aligned} \quad (32)$$

The following Lyapunov function is adopted,

$$\begin{aligned} V &= \frac{1}{2} s^T M_r s + \frac{1}{2} \text{tr}(\widetilde{W}_{M_r}^T Q_{M_r} \widetilde{W}_{M_r} + \widetilde{W}_{C_r}^T Q_{C_r} \widetilde{W}_{C_r} \\ &\quad + \widetilde{W}_{G_r}^T Q_{G_r} \widetilde{W}_{G_r} + \widetilde{W}_f^T Q_f \widetilde{W}_f) \end{aligned} \quad (33)$$

where $Q_{M_r}, Q_{C_r}, Q_{G_r}, Q_f$ are positive definite weight matrices. $\text{tr}(\bullet)$ means the trace of the matrix. $\widetilde{W}_{(\cdot)} = W_{(\cdot)} - \widehat{W}_{(\cdot)}$, the (33) can be further derived as below,

$$\begin{aligned} \dot{V} &= -s^T K_r^q s - s^T \varrho_f - \text{tr}[\widetilde{W}_{M_r}^T (Z_{M_r} \dot{v} s^T + Q_{M_r} \widehat{W}_{M_r})] \\ &\quad - \text{tr}[\widetilde{W}_{C_r}^T (Z_{C_r} v s^T + Q_{C_r} \widehat{W}_{C_r})] \\ &\quad - \text{tr}[\widetilde{W}_{G_r}^T (Z_{G_r} s^T + Q_{G_r} \widehat{W}_{G_r})] \\ &\quad - \text{tr}[\widetilde{W}_f^T (Z_f s^T + Q_f \widehat{W}_f)] \end{aligned} \quad (34)$$

Therefore, the neural learning updating law is designed as:

$$\begin{aligned} \dot{\widehat{W}}_{M_r} &= -Q_{M_r}^{-1} (E_{M_r} \dot{v} s^T + \beta_{M_r} \widehat{W}_{M_r}) \\ \dot{\widehat{W}}_{C_r} &= -Q_{C_r}^{-1} (E_{C_r} v s^T + \beta_{C_r} \widehat{W}_{C_r}) \\ \dot{\widehat{W}}_{G_r} &= -Q_{G_r}^{-1} (E_{G_r} s^T + \beta_{G_r} \widehat{W}_{G_r}) \\ \dot{\widehat{W}}_f &= -Q_f^{-1} (E_f s^T + \beta_f \widehat{W}_f) \end{aligned} \quad (35)$$

where $\beta_{M_r}, \beta_{C_r}, \beta_{G_r}$ and β_f are positive parameters needed to be designed. By substituting (35) into (34), we have

$$\begin{aligned} \dot{V} &= -s^T K_r^q s - s^T \varrho_f + \text{tr}[\beta_{M_r} \widetilde{W}_{M_r}^T \widehat{W}_{M_r}] \\ &\quad + \text{tr}[\beta_{C_r} \widetilde{W}_{C_r}^T \widehat{W}_{C_r}] + \text{tr}[\beta_{G_r} \widetilde{W}_{G_r}^T \widehat{W}_{G_r}] + \text{tr}[\beta_f \widetilde{W}_f^T \widehat{W}_f] \end{aligned} \quad (36)$$

According to [29], we can have a result that

$$\begin{aligned} \dot{V} &\leq -(K_r^q - \frac{1}{2}) \|s\|^2 + \Upsilon - \frac{\beta_{M_r}}{2} \|\widetilde{W}_{M_r}\|_F^2 \\ &\quad - \frac{\beta_{C_r}}{2} \|\widetilde{W}_{C_r}\|_F^2 - \frac{\beta_{G_r}}{2} \|\widetilde{W}_{G_r}\|_F^2 - \frac{\beta_f}{2} \|\widetilde{W}_f\|_F^2 \end{aligned} \quad (37)$$

where $\Upsilon = \frac{\beta_{M_r}}{2} \|W_{M_r}\|_F^2 + \frac{\beta_{C_r}}{2} \|W_{C_r}\|_F^2 + \frac{\beta_{G_r}}{2} \|W_{G_r}\|_F^2 + \frac{\beta_f}{2} \|W_f\|_F^2 + \frac{1}{2} \kappa^2$, and κ denotes the upper limit of $\|\beta_f\|$.

In addition, the $\widetilde{W}_{M_r}, \widetilde{W}_{C_r}, \widetilde{W}_{G_r}, \widetilde{W}_f$ and s satisfy the following inequality,

$$\begin{aligned} \Upsilon &\leq (K_r^q - \frac{1}{2}) \|s\|^2 + \frac{\beta_{M_r}}{2} \|\widetilde{W}_{M_r}\|_F^2 + \frac{\beta_{C_r}}{2} \|\widetilde{W}_{C_r}\|_F^2 \\ &\quad + \frac{\beta_{G_r}}{2} \|\widetilde{W}_{G_r}\|_F^2 + \frac{\beta_f}{2} \|\widetilde{W}_f\|_F^2 \end{aligned} \quad (38)$$

Substituting (38) into (37), we can make a conclusion that the robot arm system is proven to be stable as the \dot{V} is a negative definite matrix $\dot{V} \leq 0$ and when t tends to infinity, s asymptotically approaches 0, i.e., q asymptotically approaches q_d , the tracking error tends to be satisfied.

V. EXPERIMENTS

In this section, the proposed method is verified through the following three steps.

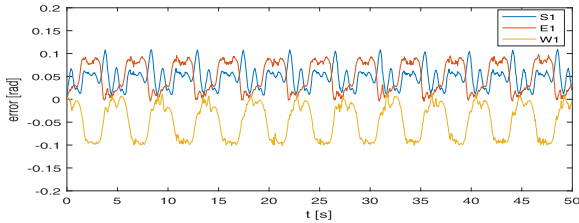


FIGURE 4. The joint angles tracking errors of the controller without neural learning.

A. TEST OF THE ADAPTIVE CONTROLLER WITH NEURAL NETWORK

The first experiment mainly focus on the tracking performance of the proposed controller which aims to compensate the unknown dynamics and uncertain payloads. We mainly focus on three joints of the Baxter robot left arm, i.e., one joint of the shoulder *S1*, one joint of the elbow *E1* and one joint of the wrist *W1*. The left arm is controlled to track a pre-determined back and forth trajectory as $x(t) = 0.1\sin(\pi t/3) + 0.7$, $y(t) = 0.25$ and $z(t) = 0.3$.

And the orientation of the robot arm is fixed as $[x, y, z, w] = [1.29, 0.07, -1.26, -0.06]$. In addition, the joint trajectory obtained with the help of the robot inverse kinematics is employed as the input of the controller. We employ $n = 3^7$ neural network nodes for $\hat{M}_r(q)$ and $\hat{G}_r(q)$, $2n = 2 \times 3^7$ nodes for $\hat{C}_r(q, \dot{q})$, $4n = 4 \times 3^7$ nodes for $\hat{f}(q, \dot{q}, v, \dot{v})$. The weight matrices are initialized as $\hat{M}_r(0) = 0 \in R^{cn \times c}$, $\hat{C}_r(0) = 0 \in R^{2cn \times c}$, $\hat{G}_r(0) = 0 \in R^{cn \times c}$ and $\hat{f}_r(0) = 0 \in R^{4cn \times c}$, where $c = 3$ denotes the amount of the controlled joints. In order to avoid the impact of PD controller on validation of the effectiveness of the adaptive controller with NN, the parameters of the PD controller are set as $K_r^q = [40.0, 45.0, 45.0, 60.0, 18.0, 8.0, 6.0]$ and $k_s = [4.44, 9.0, 5.625, 3.75, 9.0, 5.33, 7.5]$.

A set of comparative experiments is implemented to verify the effectiveness of the proposed method. Firstly, a tracking task without neural learning is conducted. The robot arm tracking error is shown in Fig. 4. According to the tracking results, we can see that the tracking error of *S1*, *E1* and *W1* is around $0 \sim 0.1$ rad, $0 \sim 0.1$ rad and $-0.1 \sim 0$ rad.

Comparatively, a tracking task with neural learning is conducted. The tracking errors of the joint angles are shown in Fig. 5. It can be observed that the tracking error is as large as the experimental result shown in Fig. 4 in the beginning and then become smaller and converge to the vicinity of zero. The overall error is around $-0.05 \sim 0.05$ rad. As we can see, the tracking performance with neural learning is satisfying and it is better than the performance of the controller without neural learning. For the purpose of understanding the effect of neural learning process, the change of the compensation torque is shown in Fig. 6.

B. TEST OF VARIABLE ADMITTANCE CONTROL

The test of fixed admittance control and the test of variable admittance control are conducted in this subsection under the left arm of the Baxter robot.

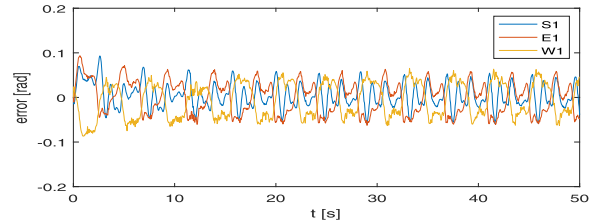


FIGURE 5. The joint angles tracking errors of the controller with neural learning.

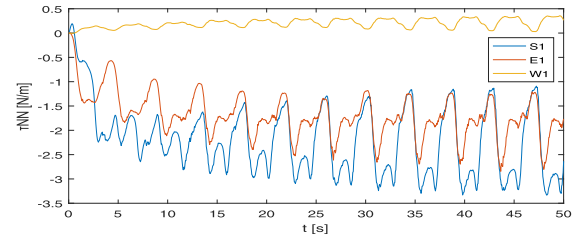


FIGURE 6. Compensation torque τ_N generated by the neural learning.

In the first test, the performance of robot arm end-effector with different fixed admittance parameters (High/Low stiffness and damping) in *y* axis is under consideration. The stiffness and damping terms of the admittance model are set as $K_r = 200\text{N/m}$, $D_r = 10\text{N/m}$ and then they turn to $K_r = 50\text{N/m}$, $D_r = 5\text{N/m}$ at 5s. Two groups of stiffness and damping terms mention above are set according to the stable range of the robot arm, reflecting the relatively high stiffness and relatively low stiffness, respectively. The robot arm trajectory is set as $0.7\text{m} \rightarrow 0.3\text{m}$ in *x* axis. The external force $F \approx 13\text{N}$ is applied in the process mentioned above at about 1.5s and 6.5s in *y* axis and it is kept for about a half second. The experiment results are shown in Fig. 7.

According to the experimental results, the influences of admittance parameters on responses of the robot arm to disturbances are reflected intuitively. At the first stage, with the high stiffness and damping, the robot arm endpoint position is dropped to 0.53m when the external force applied. At the second stage, with the low stiffness and damping, the robot arm endpoint position is dropped to 0.398m when the external force applied. The robot arm with high stiffness and damping is less affected, and we can also see that the trajectory of axis *Y* suffered less interference. In this case, giving the end-effector of the robot arm high stiffness and damping in directions without movement in a human-robot collaboration task can strengthen the stability and enhance the performance.

In the second test, the performance of robot arm end-effector with variable admittance parameters in $x'(y')$ axis is under consideration. A comparative test which simulate the pulling back process is conducted to verify the validity of the variable admittance control method. The scenario of this experiment is that the operator brakes suddenly with high endpoint stiffness and damping in the process of the saw pulling back. And we track the interaction force and position to verify the proposed method. The robot arm trajectory

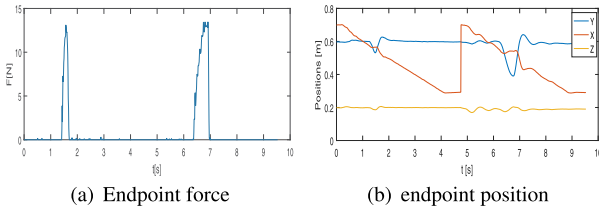


FIGURE 7. The external force applied in y axis and the position of the robot arm end-effector.

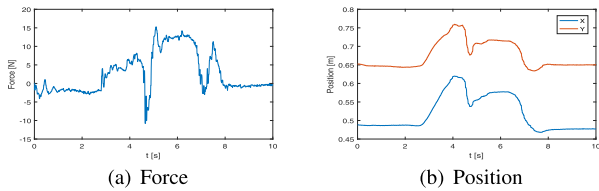


FIGURE 8. The interaction force in x axis and the position of the end-effector with fixed high admittance parameters.

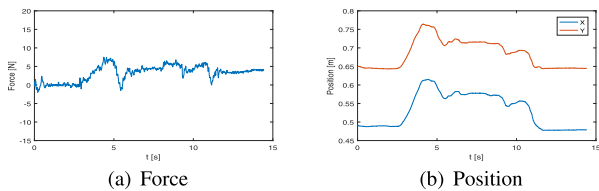


FIGURE 9. The interaction force in x axis and the position of the end-effector with variable admittance parameters.

targets are set as $0.76m$ to $0.65m$ in x axis and $0.62m$ to $0.48m$ in y axis. Thus the initial position x'_0 is set as $0.98m$ and the trajectory task goal is $0.98m$ to $0.81m$. The robot arm reference trajectory is determined by (16) with $U = 1$ and $V = 0.81$. Therefore, the reference endpoint trajectory is $x_f = 0.81 + 0.18e^{-t}$ and its goal position is $x_f = 0.81m(t \rightarrow \infty)$.

The experimental results are shown in Fig. 8 and Fig. 9. Fig. 8 shows the interaction force and endpoint trajectory of the robot arm with fixed high admittance parameters. We can see that the operator brakes suddenly at about $5s$ and the interaction force changes from $5N$ to $-10N$ and it bounces back to about $15N$. It is obvious that the change range of the interaction force is too large and it would cause unnecessary vibrations. Fig. 9 shows the interaction force and endpoint trajectory of the robot arm with variable admittance parameters. With the help of variable admittance control, the robot arm admittance model changes corresponding to the impedance of the human arm. Once the operator's arm suddenly becomes rigid, the admittance parameters of the robot arm shrink in order to cater to the operator's changes. As a result, we can see that the operator brakes suddenly at about $5s$ and $9s$ and the interaction force changes from about $5N$ to $0N$ and it bounces back to about $4N$. Fig. 8(b) shows that when the operator braked at about $5s$, the position dropped from $0.75m$ to $0.66m$ in Y axis and $0.62m$ to $0.53m$ in X axis, which corresponding to the high interaction force between the robot arm and human arm at about $5s$ in Fig.8(a). In addition, Fig. 9(b) shows

the smooth braking process with variable admittance control. This test shows that variable admittance control can resulting in a satisfied balance between the interaction force and the robot arm end-effector position.

C. HUMAN-ROBOT COLLABORATIVE SAWING TASK

Based on general experience, the performance of two-person sawing task under master-slave structure would be better. In this case, the human-robot collaborative sawing task can be split into two stages. In the first stage, the operator plays the role of the master to pull the saw along the blade and the robot arm is compliant to the master in the motion axis in order not to oppose operator's effort. And in the second stage, the robot arm is changed to be the master to pull the saw along the blade and the operator is compliant to the robot arm in turn.

In this subsection, a set of cooperative experiment is conducted to verify the proposed control method. Fig. 1 shows the experiment setup, the extracted human arm configurations and the muscle activation level data are used to regulate the human arm impedance parameters and the endpoint stiffness of the human arm is utilized to map the joint stiffness of the robot arm. And the force feedback is employed as the input of the robot arm endpoint admittance control model.

For convenience, the robot endpoint task goal in $x'(y')$ axis is predetermined at a point $x = 0.75m$ and $y = 0.65m$. Therefore, the robot arm pull the saw to the task goal when it is robot arm's turn to be master. Conversely, when the human arm pull back the saw, the robot arm is compliant and allows the human arm to pull the saw to anywhere within the control range. The rotational stiffness of the human arm endpoint is set at a high value $K_{Hrot} = 1000N/m$ in order to maintain the orientation of the robot arm end-effector with a high mapping rotational joint stiffness. According to the test of fixed admittance control results, the parameters of the admittance model along the direction perpendicular to the direction of motion $x'(y')$ are set in high stiffness and damping in order to avoid the interference with the sawing performance.

The first experiment is conducted utilizing fixed high-low stiffness switching method. In this case, the stiffness of each joint can be set to arbitrary value under the premise of stability. According to the actual situation, the stiffness of joint $S1$ is fixed as $K_{max} = 200Nm/rad$ and $K_{min} = 50Nm/rad$, the stiffness of joint $E1$ is fixed as $K_{max} = 150Nm/rad$ and $K_{min} = 40Nm/rad$ and the stiffness of joint $W1$ is fixed as $K_{max} = 35Nm/rad$ and $K_{min} = 10Nm/rad$. The trigger value of the stiffness switching is $K_x = 1kN/m$, which means that the robot joint stiffness switch to maximum value when the human arm stiffness $K_x \geq 1$ and it switch back to minimum when the $K_x \leq 1$.

The results of the first experiment are shown in Fig. 10. The first figure shows the estimated human arm endpoint stiffness while the second figure shows the stiffness of three key joint $S1$, $E1$ and $W1$ using in sawing task. The stiffness of the robot joint $S1$, $E1$ and $W1$ switch to $200Nm/rad$, $150Nm/rad$ and $35Nm/rad$ when the human arm stiffness $K_x \geq 1$ and

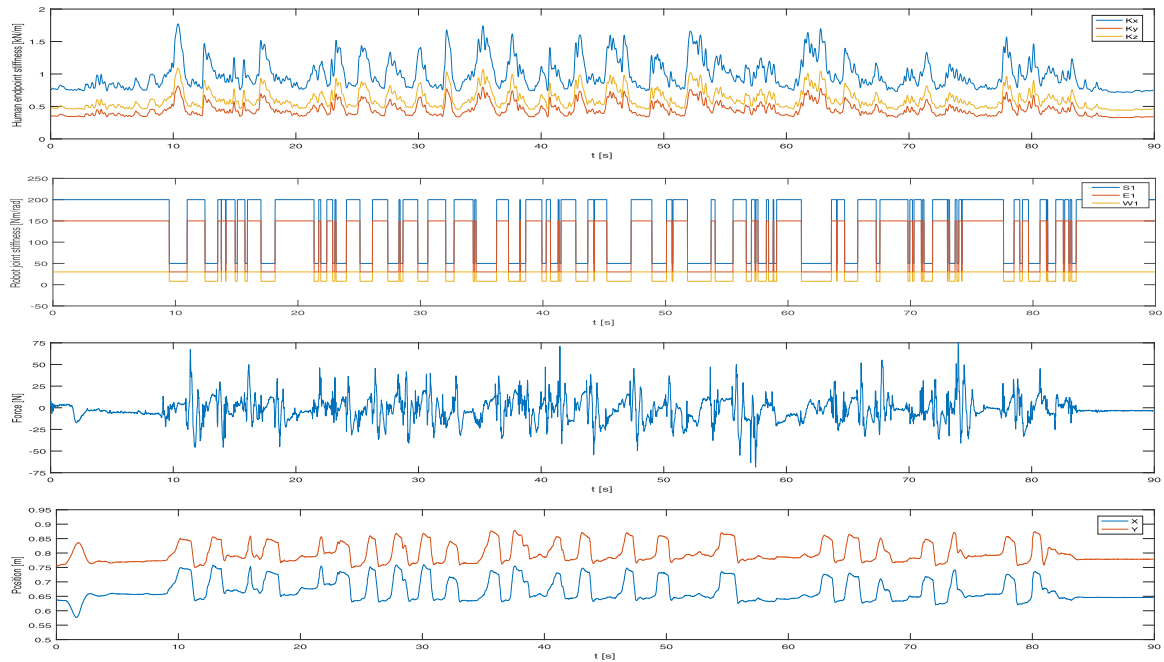


FIGURE 10. The results of human-robot collaborative sawing task using high-low stiffness switching method. First figure shows estimation of human arm endpoint stiffness. Second figure shows the stiffness of three key joint using in sawing task. Third figure shows the interaction force between human arm endpoint and robot arm end-effector. Fourth figure shows the position of the robot arm end-effector in Cartesian space.

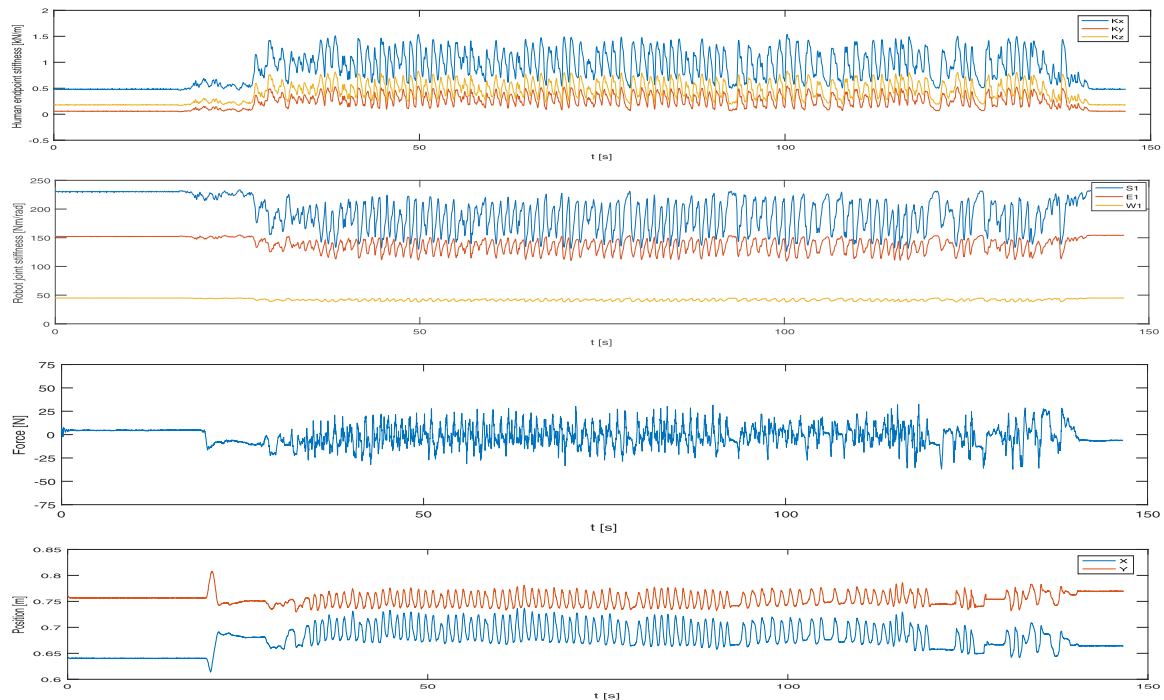


FIGURE 11. The results of human-robot collaborative sawing task using the proposed method. First figure shows estimation of human arm endpoint stiffness. Second figure shows the mapping stiffness of three key joint using in sawing task. Third figure shows the interaction force between human arm endpoint and robot arm end-effector. Fourth figure shows the position of the robot arm end-effector in Cartesian space.

they switch back to 50Nm/rad , 40Nm/rad and 10Nm/rad when $K_x \leq 1$. These two figures reflect the master-slave structure of human-robot collaborative sawing task. The third

figure shows the interaction force between human arm endpoint and robot arm end-effector. We can see the interaction force at the switching point, for example at about 11 s and 12 s,

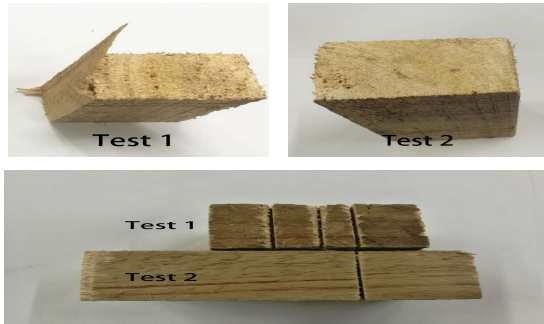


FIGURE 12. Sawing surface and vertical view of the wood. Test 1 denotes the results of the high-low stiffness switching method while Test 2 shows the results of the proposed method.

it bounces to $67N$ and drops down to $-46N$. The interaction force is very high at the switching moment, and it would cause the feeling of discomfort to the operator. In addition, the sawing performance will also be affected. The fourth shows the position of robot arm end-effector in Cartesian space. According to the Fig. 10, we can see that the sawing performance is not smooth enough and the blade is stuck at about $55s$ in the sawing process.

The second experiment is conducted using the proposed method. The robot arm joint stiffness change corresponding to the human arm endpoint stiffness in real time. According to the test of variable admittance control method, this method is employed in the process of robot arm pulling back.

The experimental results are shown in Fig. 11. The first and second figures show the estimated human arm endpoint stiffness and the mapping stiffness of the three key joint based on (10) and the constant matrix K_r^a is set as $diag\{230, 150, 50\}$. The third figure shows the interaction force during the sawing process. We can see that the interaction force is maintained between $25N$ and $-25N$ during the master-slave transition moments. The fourth and fifth figures show the position of the robot arm end-effector. Since the direction of sawing task is along the $x'(y')$ axis, we present the position of X axis and Y axis as an alternative. According to the Fig. 11, it is obvious that the sawing performance of the proposed method is much smoother than the performance of high-low stiffness switching method, the interaction force would not bounce or drop down to a very high level with the control law of the admittance model. We can observe from the third and fourth figures at about $75s$ to $110s$ that the operator is allowed to increase or decrease the sawing frequency, or even stop and resume sawing task at any time (the smooth curve at about $125s$ and $135s$ in the fourth figure). And the interaction force would not vary greatly during the stop and resume process.

The intuitive results of the human-robot collaborative wood sawing task are shown in Fig. 12. Test 1 denotes the results of the high-low stiffness switching method while Test 2 shows the results of the proposed method. With the proposed method, the object has a smoother sawing surface and less wood burrs.

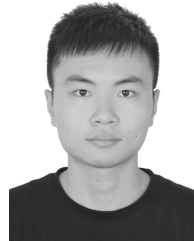
VI. CONCLUSION

In this paper, a novel neural learning enhanced variable admittance control approach was proposed for the human-robot collaboration task. Firstly, the human arm impedance parameters were estimated by recording the EMG signals and tracking the arm configurations. The estimated endpoint stiffness of the human arm was used to map the joint stiffness of the robot arm and the full impedance parameters of the human arm were employed to obtain the corresponding admittance model of the robot arm. In order to enhance the tracking performance of the robot arm, a NN-based adaptive controller was designed to compensate for the unknown dynamics and uncertain payloads. The validity of the proposed technique was verified by comparative experiments. In our future study, we will consider to improve the proposed approach for more complex tasks. In this paper, the EMG signals is used to monitor the muscle activation levels and we will also try to combine with the muscle fatigue measurement method into our framework in the future study.

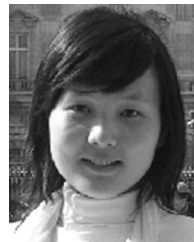
REFERENCES

- [1] Y. Li and S. S. Ge, "Human-robot collaboration based on motion intention estimation," *IEEE/ASME Trans. Mechatronics*, vol. 19, no. 3, pp. 1007–1014, Jun. 2014.
- [2] W. Kim, J. Lee, L. Peternel, N. Tzarakis, and A. Ajoudani, "Anticipatory robot assistance for the prevention of human static joint overloading in human-robot collaboration," *IEEE Robot. Autom. Lett.*, vol. 3, no. 1, pp. 68–75, Jan. 2018.
- [3] W. He, X. He, M. Zou, and H. Li, "PDE model-based boundary control design for a flexible robotic manipulator with input backlash," *IEEE Trans. Control Syst. Technol.*, vol. 27, no. 2, pp. 790–797, Mar. 2019.
- [4] Z. Li, W. Yuan, S. Zhao, Z. Yu, Y. Kang, and C. L. P. Chen, "Brain-actuated control of dual-arm robot manipulation with relative motion," *IEEE Trans. Cogn. Develop. Syst.*, vol. 11, no. 1, pp. 51–62, Mar. 2019.
- [5] Z. Li, C. Deng, and K. Zhao, "Human-cooperative control of a wearable walking exoskeleton for enhancing climbing stair activities," *IEEE Trans. Ind. Electron.*, vol. 67, no. 4, pp. 3086–3095, Apr. 2020.
- [6] C. Yang, G. Ganesh, S. Haddadin, S. Parusel, A. Albu-Schaeffer, and E. Burdet, "Human-like adaptation of force and impedance in stable and unstable interactions," *IEEE Trans. Robot.*, vol. 27, no. 5, pp. 918–930, Oct. 2011.
- [7] W. He and Y. Dong, "Adaptive fuzzy neural network control for a constrained robot using impedance learning," *IEEE Trans. Neural Netw. Learn. Syst.*, vol. 29, no. 4, pp. 1174–1186, Apr. 2018.
- [8] R. Lozano and B. Brogliato, "Adaptive hybrid force-position control for redundant manipulators," *IEEE Trans. Autom. Control*, vol. 37, no. 10, pp. 1501–1505, Oct. 1992.
- [9] W. He, T. Meng, X. He, and S. S. Ge, "Unified iterative learning control for flexible structures with input constraints," *Automatica*, vol. 96, pp. 326–336, Oct. 2018.
- [10] J. Craig and M. Raibert, "A systematic method of hybrid position/force control of a manipulator," in *Proc. COMPASAC 79. Comput. Softw. IEEE Comput. Soc. 3d Int. Appl. Conf.*, Aug. 2005, pp. 446–451.
- [11] W. He, T. Meng, X. He, and C. Sun, "Iterative learning control for a flapping wing micro aerial vehicle under distributed disturbances," *IEEE Trans. Cybern.*, vol. 49, no. 4, pp. 1524–1535, Apr. 2019.
- [12] K. Wen, D. Neculescu, and G. Basic, "Development system for a haptic interface based on impedance/admittance control," in *Proc. 2nd Int. Conf. Creating, Connecting Collaborating Through Comput.*, Feb. 2005, pp. 147–151.
- [13] I. Ranatunga, F. L. Lewis, D. O. Popa, and S. M. Toussef, "Adaptive admittance control for human-robot interaction using model reference design and adaptive inverse filtering," *IEEE Trans. Control Syst. Technol.*, vol. 25, no. 1, pp. 278–285, Jan. 2017.
- [14] A. Lecours, B. Mayer-St-Onge, and C. Gosselin, "Variable admittance control of a four-degree-of-freedom intelligent assist device," in *Proc. IEEE Int. Conf. Robot. Autom.*, May 2012, pp. 3903–3908.

- [15] S. S. Ge, Y. Li, and C. Wang, "Impedance adaptation for optimal robot-environment interaction," *Int. J. Control*, vol. 87, no. 2, pp. 249–263, Feb. 2014.
- [16] C. Zeng, C. Yang, J. Zhong, and J. Zhang, "Encoding multiple sensor data for robotic learning skills from multimodal demonstration," *IEEE Access*, vol. 7, pp. 145604–145613, 2019.
- [17] T. Tsumugiwa, R. Yokogawa, and K. Hara, "Variable impedance control based on estimation of human arm stiffness for human-robot cooperative calligraphic task," in *Proc. IEEE Int. Conf. Robot. Autom.*, Jun. 2003, pp. 644–650.
- [18] Z. Li, Y. Yuan, F. Ke, W. He, and C.-Y. Su, "Robust Vision-Based Tube Model Predictive Control of Multiple Mobile Robots for Leader-Follower Formation," *IEEE Trans. Ind. Electron.*, vol. 67, no. 4, pp. 3096–3106, Apr. 2020.
- [19] D. J. Agravante, A. Cherubini, A. Bussy, P. Gergondet, and A. Kheddar, "Collaborative human-humanoid carrying using vision and haptic sensing," in *Proc. IEEE Int. Conf. Robot. Autom. (ICRA)*, May 2014, pp. 607–612.
- [20] L. Peternel, N. Tsagarakis, and A. Ajoudani, "A human-robot co-manipulation approach based on human sensorimotor information," *IEEE Trans. Neural Syst. Rehabil. Eng.*, vol. 25, no. 7, pp. 811–822, Jul. 2017.
- [21] Z. Li, J. Li, S. Zhao, Y. Yuan, Y. Kang, and C. L. P. Chen, "Adaptive neural control of a kinematically redundant exoskeleton robot using brain-machine interfaces," *IEEE Trans. Neural Netw. Learn. Syst.*, vol. 30, no. 12, pp. 3558–3571, Dec. 2019.
- [22] Z. Li, Y. Yuan, L. Luo, W. Su, K. Zhao, C. Xu, J. Huang, and M. Pi, "Hybrid brain/muscle signals powered wearable walking exoskeleton enhancing motor ability in climbing stairs activity," *IEEE Trans. Med. Robot. Bionics*, vol. 1, no. 4, pp. 218–227, Nov. 2019.
- [23] J. R. Medina, M. Shelley, D. Lee, W. Takano, and S. Hirche, "Towards interactive physical robotic assistance: Parameterizing motion primitives through natural language," in *Proc. IEEE RO-MAN, 21st IEEE Int. Symp. Robot Hum. Interact. Commun.*, Sep. 2012, pp. 1097–1102.
- [24] P. Evrard, E. Gribovskaya, S. Calinon, A. Billard, and A. Kheddar, "Teaching physical collaborative tasks: Object-lifting case study with a humanoid," in *Proc. 9th IEEE-RAS Int. Conf. Humanoid Robots*, Dec. 2009, pp. 399–404.
- [25] A. Gams, B. Nemeč, A. J. Ijspeert, and A. Ude, "Coupling movement primitives: Interaction with the environment and bimanual tasks," *IEEE Trans. Robot.*, vol. 30, no. 4, pp. 816–830, Aug. 2014.
- [26] C. Yang, C. Zeng, P. Liang, Z. Li, R. Li, and C.-Y. Su, "Interface design of a physical human-robot interaction system for human impedance adaptive skill transfer," *IEEE Trans. Autom. Sci. Eng.*, vol. 15, no. 1, pp. 329–340, Jan. 2018.
- [27] P. Artemiadis and K. Kyriakopoulos, "EMG-based control of a robot arm using low-dimensional embeddings," *IEEE Trans. Robot.*, vol. 26, no. 2, pp. 393–398, Apr. 2010.
- [28] A. Ajoudani, *Teleimpedance: Teleoperation with Impedance Regulation Using a Body-Mach. Interface*. Thousand Oaks, CA, USA: Sage Publications, 2012.
- [29] C. Yang, X. Wang, L. Cheng, and H. Ma, "Neural-Learning-Based Telerobot Control With Guaranteed Performance," *IEEE Trans. Cybern.*, vol. 47, no. 10, pp. 3148–3159, Oct. 2017.
- [30] X. Ren, A. B. Rad, and F. L. Lewis, "Neural network-based compensation control of robot manipulators with unknown dynamics," in *Proc. Amer. Control Conf.*, Jul. 2007, pp. 13–18.
- [31] B. Yang, H. Lu, and L. Chen, "BPNN and RBFNN based modeling analysis and comparison for cement calcination process," in *Proc. 3rd Int. Workshop Adv. Comput. Intell.*, Aug. 2010, pp. 101–106.
- [32] A. Ajoudani, C. Fang, N. G. Tsagarakis, and A. Bicchi, "A reduced-complexity description of arm endpoint stiffness with applications to teleimpedance control," in *Proc. IEEE/RSJ Int. Conf. Intell. Robots Syst. (IROS)*, Sep. 2015, pp. 1017–1023.
- [33] R. Johansson and M. Spong, "Quadratic optimization of impedance control," in *Proc. IEEE Int. Conf. Robot. Autom.*, Dec. 2002, pp. 616–621.
- [34] M. Matinfar and K. Hashtrudi-Zaad, *Optimization-based Robot Compliance Control: Geometric and Linear Quadratic Approaches*. Thousand Oaks, CA, USA: Sage Publications, 2005.
- [35] X. Chen, C. Yang, C. Fang, and Z. Li, "Impedance matching strategy for physical human robot interaction control," in *Proc. 13th IEEE Conf. Autom. Sci. Eng. (CASE)*, Aug. 2017, pp. 138–144.
- [36] C. Fang and X. Ding, "A Set of Basic Movement Primitives for Anthropomorphic Arms," in *Proc. IEEE Int. Conf. Mechatron. Autom.*, Aug. 2013, pp. 639–644.
- [37] X. Ding and C. Fang, "A novel method of motion planning for an anthropomorphic arm based on movement primitives," *IEEE/ASME Trans. Mechatron.*, vol. 18, no. 2, pp. 624–636, Apr. 2013.



XIONGJUN CHEN received the B.Eng. degree in automation from the South China University of Technology, Guangzhou, China, in 2017, where he is currently pursuing the M.S. degree. His current research interests include human-robot interaction, machine learning, and data mining.



NING WANG (Member, IEEE) received the B.Eng. degree in measurement and control technologies and devices from the College of Automation, Northwestern Polytechnical University, Xi'an, China, in 2005, and the M.Phil. and Ph.D. degrees in electronic engineering from the Department of Electronic Engineering, The Chinese University of Hong Kong, Hong Kong, in 2007 and 2011, respectively. She is currently a Senior Lecturer with the University of the West of England, Bristol. Her research interests are in signal processing and machine learning, with applications in robust speaker recognition, pattern recognition, and human-robot interaction.



HONG CHENG (Senior Member, IEEE) is currently a Professor of the School of Automation of Engineering, University of Electronic Science and Technology of China, Chengdu, China. His current research interests include computer vision and machine learning, robotics, human-computer interaction, and multimedia signal processing. He is a Senior Member of ACM and an Associate Editor of the *IEEE Computational Intelligence Magazine*.



CHENGUANG YANG (Senior Member, IEEE) received the Ph.D. degree in control engineering from the National University of Singapore, Singapore, in 2010. He performed a Postdoctoral Research in human robotics with Imperial College London, London, U.K., from 2009 to 2010. He is currently a Professor of robotics with the University of the West of England, Bristol. His research interests are in human-robot interaction and intelligent system design. He has been awarded the EU Marie Curie International Incoming Fellowship, the U.K. EPSRC UKRI Innovation Fellowship, the Best Paper Award of the IEEE TRANSACTIONS ON ROBOTICS, and over ten conference Best Paper Awards.